HOT ELECTRON SCALING AND ENERGY COUPLING IN NONLINEAR LASER PLASMA INTERACTIONS

Final Report

Prepared for the
U.S. Department of Energy
under Contract No. DE-SC0014594

HOT ELECTRON SCALING AND ENERGY COUPLING IN NONLINEAR LASER PLASMA INTERACTIONS

FINAL REPORT COVER PAGE

DOE Award Number:	DE-SC0014594
Recipient Institution:	University of California
Project Title:	Hot Electron Scaling and Energy Coupling in Nonlinear Laser Plasma Interactions
Principal Investigator (PI) name and contact information:	Farhat Beg Center for Energy Research University of California San Diego San Diego, CA 92093 (858) 822-1266 fbeg@ucsd.edu
Project Period:	August 15, 2015 to February15, 2019
Reporting Period:	August 15, 2015 to February 15, 2019
Report submission date:	January 5, 2020
This project was collaboration between University of California, San Diego (UCSD) and General Atomics with GA as the lead institution	

JANUARY 5, 2020

1. PROJECT GOALS AND OBJECTIVES

Energy conversion from high power lasers to energetic hot electrons is a fundamental phenomenon in laser-plasma interactions. At laser intensities above a few times 10^{14} W/cm^2, nonlinear laser-plasma interactions lead to the generation of hot electrons with a broad energy distribution at typical temperatures of 10's – 100's kilo-electron-volt (keV). The fraction of laser energy transferred to hot electrons, their energy distribution and energy coupling efficiency to the targets are strongly affected by the laser intensity, wavelength and the plasma condition. Most investigations to date that are related to the fusion of high-energy-density laboratory plasmas (HEDLP) are carried out with relatively moderate laser intensity and lower laser wavelength to minimize hot electron generation, as electron preheating can degrade the fuel assembly. An alternative fusion scheme known as shock ignition (SI) [1] has been proposed, requiring a high intensity spike pulse at the end of a fuel assembly phase to generate a strong shock to ignite the fuel. An initial shock pressure of 0.3 Gbar is required for ignition-scale targets using the SI scheme, requiring a relatively high on-target laser intensity of 5-10×10^{15} W/cm^2 for the spike pulse. At such intensities, copious hot electrons can be produced by laser-plasma-instabilities (LPI), e.g., Stimulated Raman Scattering (SRS) and Two-Plasmon Decay (TPD). While very energetic electrons (>200 keV) could preheat the fuel, electrons with moderate energies may actually be beneficial for the SI scheme. Electrons in the 50-100 keV range can be stopped in the compressed high-density outer ablator layer leading to an increase in the ignitor shock strength and therefore enhancing overall efficiency [2-5] in the SI scheme. Considering this importance of total energy and temperature of hot electrons, it is necessary to understand the LPI in the SI high intensity regime. Characterizing the hot electron source and energy coupling is key to investigating the viability of the SI concept.

The overall goal of the HEDLP award was to perform a detailed study of the scaling of hot electron generation and energy coupling on high power laser systems, with intensity, wavelength, and target ablator material relevant to the nonlinear laser-plasma interaction at SI relevant conditions. This was a collaborative project between the Center for Energy Research at the University of California, San Diego (UCSD) and General Atomics. The experiment was performed at the Omega Laser Facility at the Laboratory for Laser Energetics (LLE) in the University of Rochester. Specific objectives of the work were to:

- understand the basic physics of laser-plasma interactions and instabilities at high laser intensities (up to 10^{17} W/cm^2) and the effects of low-Z ablator materials and laser wavelengths (IR pulse at 1.054 μm versus UV pulse at 0.351 μm) and intensity scaling
- fully characterize the resultant hot electron energy distribution
- validate hot electron energy deposition via collisional and kinetic processes in the target and the induced shocks in support of electron-assisted SI concept

This work significantly extended hot electron studies beyond those previously demonstrated for SI, which were limited by the spike pulse energy (intensity) and plasma conditions. The OMEGA EP configuration allowed us to reach necessary intensity regimes with both UV and IR beams for planar geometry experiments. An integrated configuration in spherical geometry using both the OMEGA 60 UV beams and the OMEGA EP IR beams was completed in 2016, obtaining excellent hot electron data with SI relevant target geometry and plasma conditions. This will be detailed in the next section, followed by the ongoing PIC modeling that is being performed in combination with the experimental work. The modeling tool contributes to understanding the underlying LPI mechanisms, subsequent intense electron beam generation and overall transport physics. Additional integrated experiments were performed in 2018.

1. PROJECT ACCOMPLISHMENTS

We have completed several experiments under SI relevant laser intensities and plasma conditions. After an initial demonstration of the high energy IR beam produced hot electrons and energy coupling in the planar target experiment on OMEGA EP, we successfully extended the study to spherical geometry targets using the joint OMEGA 60 UV beams and OMEGA EP IR beams.

2.1.1 Experimental setup

We performed a joint experiment using the OMEGA-60 UV beams and OMEGA EP IR beams at high intensity in the OMEGA chamber in order to evaluate hot electron production and energy coupling to a spherical target with SI-relevant long scale-length hot plasmas. Six total joint shots were completed to evaluate the IR beam interaction with the long scale coronal plasma and the resultant fast electron beam generation and spatial energy deposition in the compressed spherical target. In addition, seven UV beam only shots examined the high intensity UV beam produced hot electrons spatial energy coupling. The experimental set-up for all shots with diagnostic lines-of-sight is shown in Fig. 1(a). In each shot, 60 UV laser beams uniformly irradiate a small spherical target (outer diameter of 485 μm) with an overlapping intensity of ~3×10^{15} W/cm^2 (18 kJ of total energy), creating a long scale-length high temperature coronal

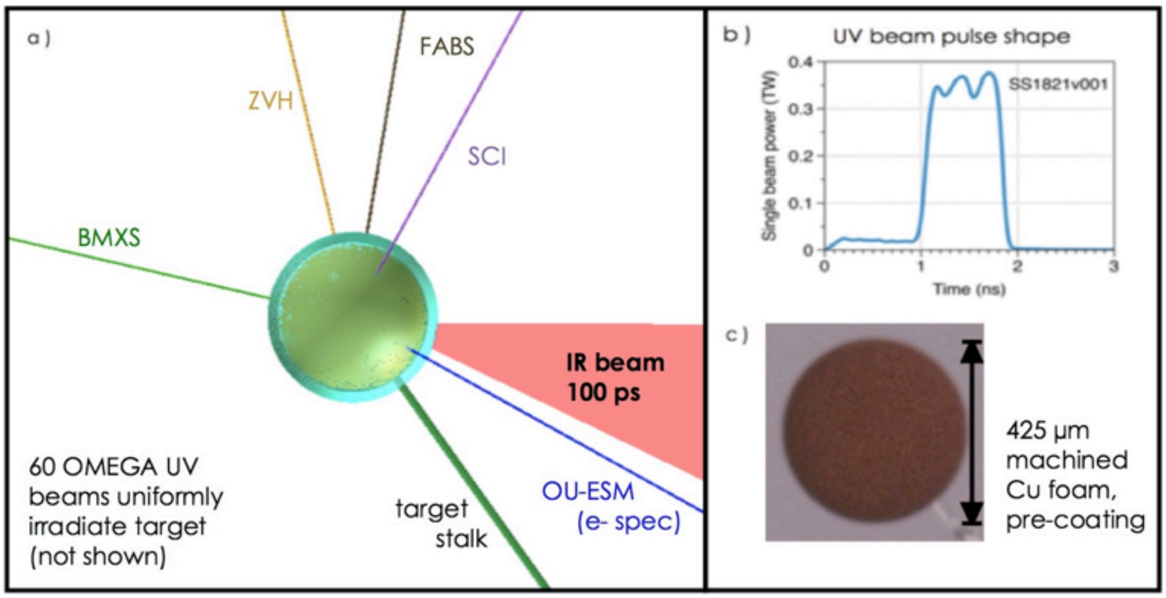

Figure 1: (a) Schematic of the joint OMEGA and OMEGA EP experiment in the OMEGA chamber and the primary diagnostics detecting hot electron-induced Cu K-shell fluorescence and Bremsstrahlung radiation; (b) pulse shape for OMEGA UV beams; (c) GA-made low-density (1.2 g/cm^3) Cu foam sphere that is coated with 30 μm of CH as ablator.

plasma (up to ~3.5 keV). The implemented pulse shape of the UV lasers, shown in Fig. 1(b), is identical to the strong spherical shock (SSS) experiments, in which over 200 Mbar ablation pressure – close to shock ignition requirement – was achieved [4,5]. This pulse starts with a low power, 0.9 ns foot to produce the long scale-length hot coronal plasma followed by the 1 ns high intensity square pulse. For the joint shots with the addition of the IR beam, the short pulse OMEGA EP laser (100 ps, ~2.7 kJ, 100 μm spot size) is injected at various time delays to the UV beams with the focal position located at either the $n_c/10$ or $n_c/4$ position (where n_c is the plasma critical density for the IR beam), guided by radiation hydrodynamic simulation results which predicted the density and temperature conditions. These variations allowed us to evaluate the dependence of i) the IR beam produced hot electron characteristics on the coronal plasma condition; ii) subsequent hot electron spatial energy coupling to the high density target on the source distance to the Cu foam sphere, and; iii) the Cu target condition (i.e., density and temperature spatial profiles that evolve with time).

To facilitate hot electron characterization, the main target consists of a low-density Cu foam sphere (425 μm in diameter) coated with a 30 μm CH acting as the ablator material. The outer diameter of the CH/Cu foam target is 485 μm. The GA-made low-density pure Cu foam (shown in Fig. 1c) with mass density of 1.2 g/cm^3 (~13.4% of solid Cu) and ~1 μm or less pore size allows for the spatial energy deposition of hot electrons to be imaged. A solid CH ball with a thin solid Cu layer (~8 μm) buried 30 μm beneath the CH ablator surface containing a comparable number of Cu atoms as the Cu foam sphere is also used for comparison.

The spatially-resolved measurement is acquired with a spherical crystal imager (SCI) [6] that creates a 2D image of the Cu Kα x-ray fluorescence emission excited by the hot electrons in the Cu foam. A separate, absolutely calibrated Zinc Von-Hamos (ZVH) x-ray spectrometer [7] using a curved HOPG crystal measures the total yield of Kα emission. A bremsstrahlung spectrometer (BMXS) [8] is also fielded to measure the hard x-ray spectrum from which we can infer the hot electron temperature and energy, in combination with a 5-channel magnet spectrometer for the escaped electron spectrum. In addition, OMEGA full aperture backscatter system (FABS) [9,10] monitors backscattering (within the laser cone) from the UV laser-plasma interaction and side-scattering (orthogonal) from the IR laser-plasma interaction.

2.1.2 FLASH simulated target plasma conditions

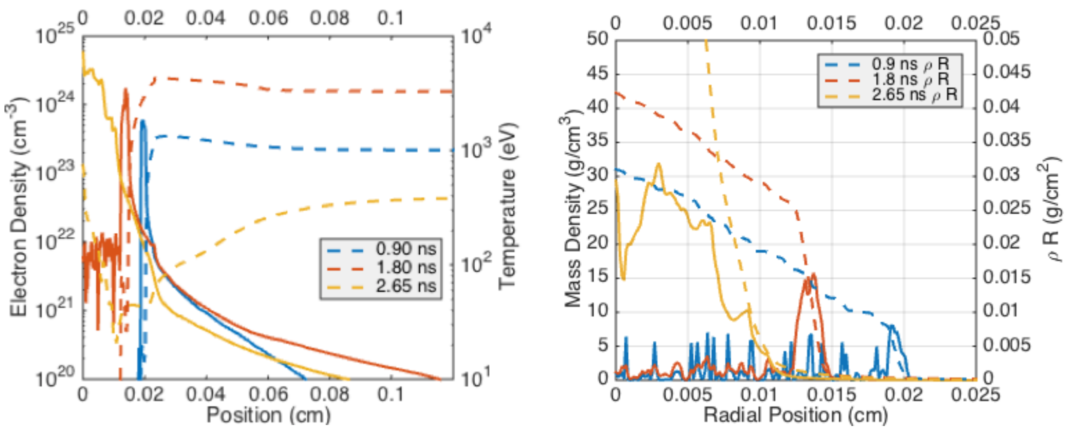

Figure 2: FLASH simulated plasma electron temperature (dash lines) and density (solid) profiles (left) and mass density and areal density (right) at 0.9, 1.8 and 2.65 ns respectively.

The radiation-hydrodynamic code FLASH [11] was used to simulate the imploded target condition including the corona plasma formation and the Cu foam compression driven by the OMEGA 60 UV lasers. These simulations were performed in 2D cylindrical symmetry with laser ray tracing modeled in 3D coordinates. The simulations used the PROPACEOS and IONMIX EOS and opacity tables of Cu and CH. Fig. 2 shows the simulated plasma temperatures and density profiles at 0.9 ns (end of the low power foot of the UV pulse), 1.8 ns (end of the UV pulse) and 2.65 ns (shock converging at the target center), respectively. One can see that plasma temperature (density scale-length) increases from 1 keV (150 μm) at 0.9 ns to 3.5 keV (450 μm) at 1.8 ns. The heated corona plasma then rapidly cools down to ~0.3 keV with a far reduced scale-length at 2.65 ns. Those simulation results were used to guide decisions of the IR beam timing with respect to the UV beams in addition to the IR beam focal position (either at $n_c/10$ or $n_c/4$) in our experiments. Simulated target conditions also facilitate data interpretation as discussed below.

2.1.3 Hot electron energy deposition in spherical targets

Our results resolved successful coupling of IR beam energy to the spherically compressing target under various laser and target conditions. Hot electron generation by the IR beam and energy coupling strongly depends on the laser plasma interaction and target conditions. Fig 3 shows Cu Kα fluorescence images on the same color-scale for three different shots: a) OMEGA-only; b) a joint shot with the IR beam focus at $n_c/10$ and delay of 0.9 ns, corresponding to the end of the low-intensity foot of the UV driver pulse; and c) a joint shot with the IR beam focus at $n_c/10$ and delay of 1.8 ns, corresponding to the end of the UV pulse. In the OMEGA-only shot, the observed Cu Kα emission spot is excited by hot electrons produced by the high intensity portion of the OMEGA UV beams (Fig. 3a). The emission has a ring-like, or horseshoe, pattern with a radius of ~150 µm, where the region of little signal corresponds to the location of the target stalk. FLASH simulations suggest that this radius corresponds to the location of the shock-compressed high density Cu foam region (Fig. 2) at the end of the UV laser pulse. UV beam produced hot electrons with energies between 50 – 100 keV [4,5] can be fully stopped in the compressed Cu foam layer with the areal density of ~25 mg/cm^2, producing a ring-like emission pattern.

In a joint shot with the OMEGA EP beam injected at 1.8 ns (Fig. 3c), the IR laser interacts with a high temperature (3.5 keV) and large scalelength (450 µm) plasma, resulting in an additional Cu Kα emission at the same radius. The localized energy deposition suggests effective stopping of IR beam produced hot electrons by the compressed Cu foam shell with areal density of 25-30 mg/cm^2, which indicates IR beam produced hot electrons having moderate energies (< ~100 keV). It should also be noted that the IR beam hot electrons induced Cu Kα emission spot has a lateral size of ~ 100 µm that is comparable

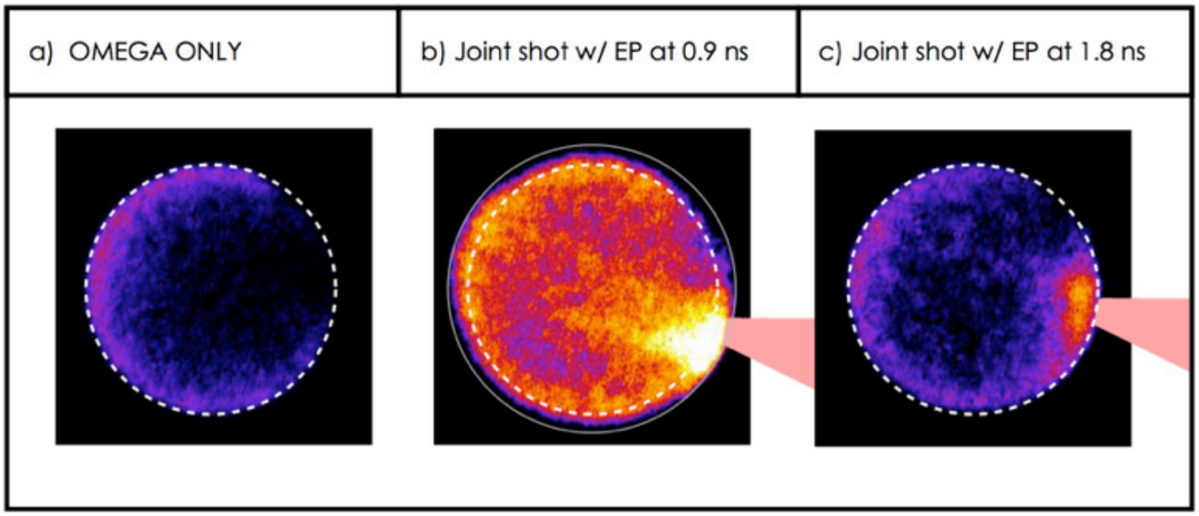

Figure 3: SCI measured Cu Kα images from an OMEGA-only shot (a), a joint OMEGA and OMEGA EP shot with the EP beam (represented by the red triangle with focal position in the corona plasma at n_c/10) at 0.9 ns (b) and a joint shot with the EP beam at 1.8 ns (c), respectively. The white dash circle has a radius of ~150 µm corresponding to the radial location of the compressed Cu foam at 1.8 ns (the end of the OMEGA driver pulse). The solid line circle in (b) has the radius of ~ 200 µm indicating the compressed Cu target size at 0.9 ns.

with the laser spot size at the n_c/10 located about 1 mm back. This would indicate a direct beam with little angular spread.

In contrast, the IR beam interaction with a shorter scalelength (~150 µm) 1 keV coronal plasma at 0.9 ns results in a much brighter Cu Kα radiation signal with a deeper penetration depth (Fig. 3b). The emission ring starts with a radius of ~200 µm which is consistent with the position of the compressed Cu foam shell at 0.9 ns in the simulation. IR beam-produced hot electrons can be seen penetrating through the compressed foam layer and transport further into the core. This can be explained by the combination of more energetic electrons due to the shorter scale-length plasma and smaller areal density (<10 mg/cm^2) of the compressed foam layer at that time, where ~100 keV and above electrons would not be stopped. It is also worth noting that the Kα emission in this case can be seen from the whole target, as evidenced by significant limb brightening. This might indicate the influence of self-generated electromagnetic fields on hot electron trajectories, which requires further investigation.

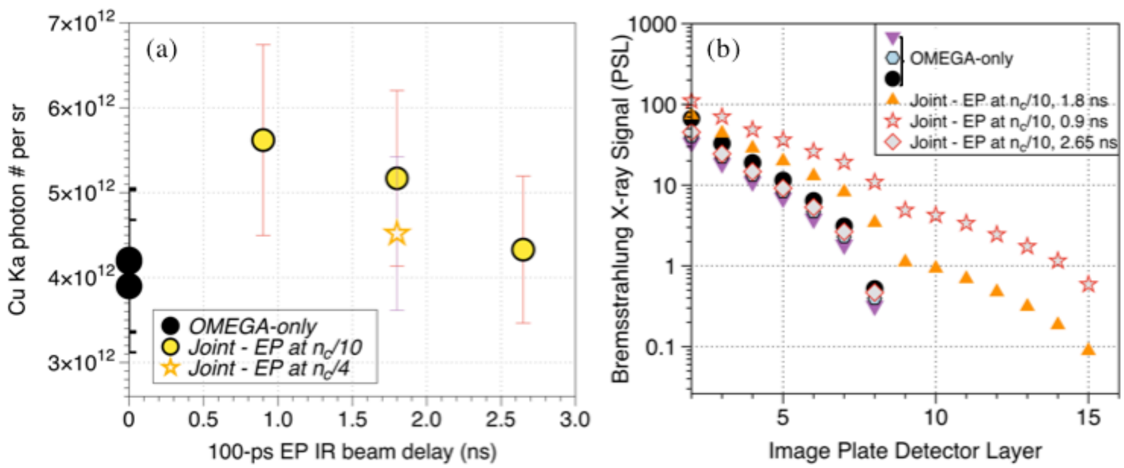

Figure 4: (a) The measured Cu Kα photon yield by the calibrated ZVH x-ray spectrometer in the shots without IR beam (black points), and with IR beam at 0.9 ns, 1.8 ns and 2.65 ns. (b) BMXS measured x-ray spectrum from 10 keV to 1 MeV, in the shots with and without EP IR beam.

The measured Cu Kα photon yield by the calibrated ZVH x-ray spectrometer, shown in Fig. 4(a), agrees with the observed SCI signal trend, that is, higher Cu Kα yield with the 0.9 ns injection time for the IR beam as compared to a 1.8 ns delay or UV beam only shots. With the same 1.8 ns delay, IR beam focusing at relatively higher density ($n_c/4$) reduces Kα x-ray emission compared to the $n_c/10$ case, suggesting potentially more beam breakup and/or filamentation. This could be attributed to a reduced hot electron number and/or a larger electron beam spread. When injecting the IR beam into a colder plasma (~300 eV) at 2.65 ns, similarly poor coupling is observed with no detectable increase in Cu Kα yield over the UV only shots. This can be explained by significant laser filamentation at low plasma temperatures. The BMXS measured hard x-ray data (Fig. 4b) show a consistent trend with the Kα data. Data analysis with the help of Monte-Carlo simulations using the GEANT4 code [12] is underway to extract information regarding the hot electron energy spectrum, temperature, and energy coupling efficiency in the target.

Fixed port FABS diagnostics measuring the UV light backscattered from the target through focusing lenses with time-resolved spectra in the region of SRS (450 – 750 nm) also captured side-scattered light from the IR beam interaction with the long scale-length plasma in all joint shots. Fig. 5 shows the temporally and spectrally-resolved backscattered light for the UV Beam #25 and side scattered light from the IR beam (94° from the IR beam axis) for the same three shot cases: (a) an OMEGA-only shot, (b) a joint shot with the OMEGA EP beam at 0.9 ns, and (c) with EP beam at 1.8 ns. Additional signal of the side-scattered light due to the OMEGA EP IR beam in the joint shots is observed to emit near its 2ω (527 nm) and also in the spectral range of 680 nm to 750 nm. The analysis of the IR side scattered light indicate the emission region in the underdense plasma in the range of 0.1 to 0.3 n_c which will be compared with the ongoing PIC simulations discussed below.

2.2 PIC MODELING OF LASER PLASMA INSTABILITIES

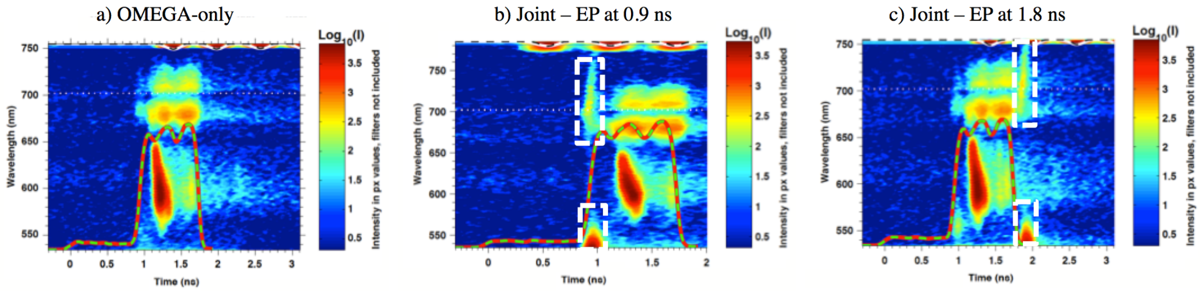

Figure 5: (a) Measured streaked SRS data in three typical shots, (a) OMEGA-only, (b) and (c) joint shots with the EP beam at 0.9 ns and 1.8 ns respectively, with the UV beam pulse overlaid on plots. Side scattered light due to the EP beam are marked in the white dashed boxes.

During this reporting period, we have performed large-scale 2D PIC simulations with the OSIRIS code [13,14] to study the laser plasma instabilities (LPI) and generated hot electrons in our planar target OMEGA-EP experiments conducted in CY15. The initial plasma conditions were obtained from the FLASH simulations. We used CH plasma with an exponential density profile from $0.1n_c$ to $0.31n_c$ (Fig. 6) which has a density scale length of 378 μm at quarter critical density $n_c/4$. The non-uniform plasma fluid velocity was also initialized. The electron and ion temperatures were 1.2 keV and 0.28 keV, respectively. The incident plane-wave laser pulse with wavelength λ=1.053μm was turned on at time=0 from the left boundary with an intensity of 5×10^{15}W/cm^2, which is estimated based on the 100 ps IR beam energy and the observed interaction spot size of ~500 μm.

Figure 6: The initial density profile of the OSIRIS simulation. The density is normalized by the n_c

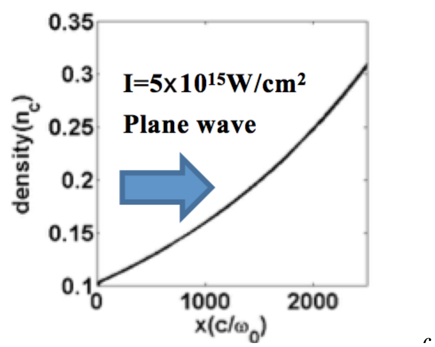

The simulation domain was rectangular with an area of 400μm×64μm. The Cartesian grid sizes dx and dy were set at $0.1c/\omega_0 = 0.017$ μm and the time step at $dt=0.0707/\omega_0=0.04$ fs, where ω_0 and c are the laser angular frequency and the speed of light. The whole simulation ran for 6 ps. The number of particles per cell was 100 for the electron species and 50 for each ion species of CH. For electromagnetic fields, we used open boundary conditions in the x (longitudinal) direction and periodic boundary conditions in the y (transverse) direction. For particles, we used thermal and periodic boundary conditions along the x and y directions, respectively. The hot electrons crossing the longitudinal boundaries were recorded to study the hot electron flux. The electrons distributed inside the simulation box with energy above 50 keV were also diagnosed to characterize the hot electrons generated by the LPI modes at different times.

A significant feature of the experimental results is the directionality of the generated hot electrons (FWHM=29°). On this point, our simulation results demonstrate the time evolution of the LPI modes and the corresponding hot electron divergence angle. When the laser pulse enters the simulation box, the first observed LPI is stimulated Raman scattering (SRS), which dominates the early stage of the simulation before the two-plasmon decay (TPD) begins to grow. Figure 7(a) shows the SRS modes at 1ps in the phase space of x and transverse wave vector k_y. SRS firstly occurs below $x=1000\ c/\omega_0$ ($0.15n_c$). The hot electrons (>50 keV) accelerated at this time are plotted in Figure 7(b) in the phase space of x and hot electron angle θ calculated from $\theta = \arctan(p_y / p_x)$, where p_y and p_x are the transverse and longitudinal momentum

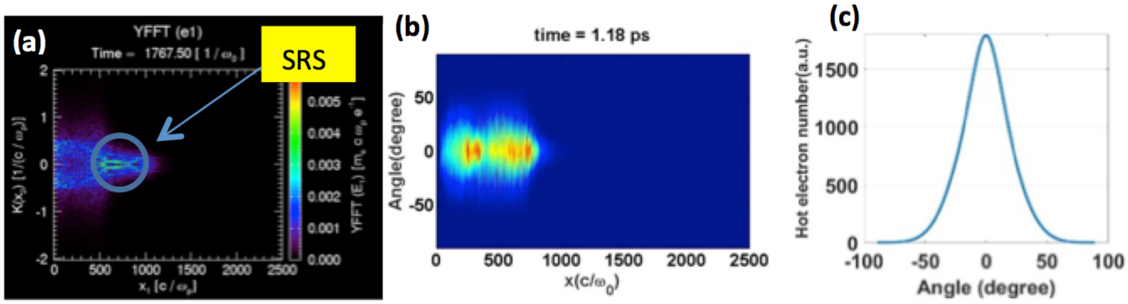

Figure 7. (a) The spectrum of the longitudinal electric field in the phase space of x and ky. (b) The hot electrons with energy above 50 keV in the phase space of x and divergence angle. (c) the integrated hot electron energy distribution from (b). All figures are at 1ps.

of hot electrons. The hot electrons generated by SRS modes have a FWHM of 40° in the angular space [Figure 7(c)]. It should be noted that the actual hot electrons should have a lower divergence angle than the calculations above because the p_y here includes an additional component from the oscillating laser field, and this component can increase the divergence angle. The small divergence angle of hot electrons is caused by the directionality of the SRS modes with moderate longitudinal wave number k_x(~1.4k_0) and very small transverse wave number k_y(~0.3k_0), where k_0 is the laser wave number in vacuum. Therefore, the typical wave vector of the SRS modes has an angle of 21° in the longitudinal direction, consistent with the FWHM of 40° of generated hot electrons.

Later at 2ps, the TPD modes begin to grow near the $n_c/4$ surface, as shown in Figure 8(a). TPD modes can be observed between x=1500~2000 c/ω$_0$ (0.2~0.25n_c) with significant transverse wave vectors. The corresponding hot electron angular distribution now is shown in Figure 8(b), in which the hot electrons generated from SRS and TPD are distinguished clearly based on their locations. Those hot electrons from SRS with x<1500 c/ω$_0$ still have the same divergence angle with that at 1ps [Figure 7(b)]. In comparison, the hot electrons from TPD with x>1500 c/ω$_0$ have wider transverse branches, suggesting a larger divergence angle. As time goes on, TPD becomes stronger, and the FWHM of the total hot electron divergence angle keeps increasing to ~100° at ~3.6ps, as recorded at the forward boundary of the simulation domain [Figure 8(c)]. This large angle agrees with the direction of the observed TPD modes near 0.2n_c with k_x~k_y=1.5k_0 and a half angle of 45° to the longitudinal direction.

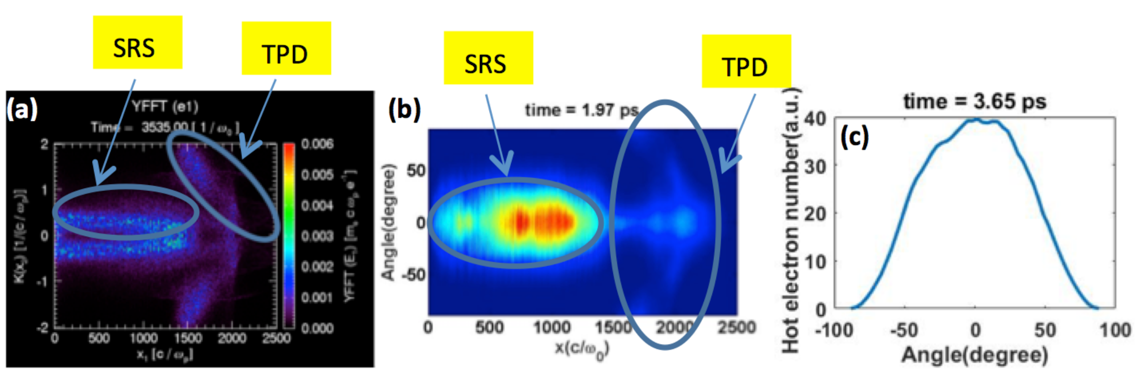

Figure 8. (a) The spectrum of the longitudinal electric field in the phase space of x and ky. (b) The hot electrons (with energy above 50 keV) in the phase space of x and divergence angle. (c) The hot electron angular distribution diagnosed at the forward boundary at 3.65ps. (a) and (b) are at 2ps.

Compared to the experimental results, our conjecture is that the dominant hot electron source in the experiment is SRS. The hot electrons generated from SRS with FWHM=40° are more consistent with the divergence angle calculated from the SCI data in the 2015 planar target experiments (FWHM=29°) than those generated from TPD (FWHM=100°). Considering the 40° of FWHM is an overestimate of the divergence angle because of the hot electron oscillation in the laser field, the actual consistency should be better.

Another simulation result supporting our conjecture is that the TPD generated hot electrons have much higher energy than that observed in the experiment. The hot electron energy fraction of the laser energy increases from 5% to 17% when TPD becomes significant at 3 ps, which is much higher than 2% from the experiments. TPD modes can more efficiently catch and accelerate the background electrons with the higher wave number and lower phase velocity than SRS modes, especially in the region away from the $n_c/4$ surface ~$0.2n_c$. This results in a higher hot electron energy flux diagnosed at the boundary of the simulation domain (Fig. 9). The strong TPD modes at 3 ps causes a peak of hot electron energy flux of 17% at ~3.6 ps. Later the number drops to 4% when TPD becomes weak because of the pump depletion of the laser energy caused by SBS and SRS. Therefore, TPD-generated hot electrons clearly have a higher energy fraction of the total laser energy than those observed in the experiment.

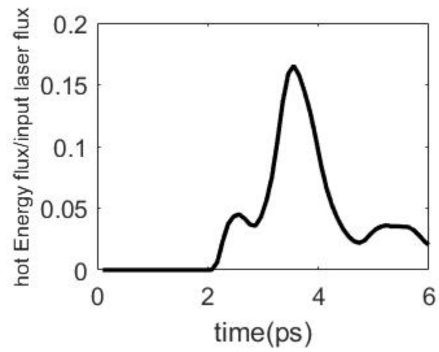

Figure 9: The time evolution of the hot electron (>50keV) energy flux at forward boundary. The data are normalized by the incident laser energy flux.

In summary, we have analyzed the LPI modes and the corresponding hot electron features in our PIC simulations. Based on the comparison between our analysis and the experimental results, we preliminarily conjecture that the dominant mechanism of hot electron generation is SRS in the 2015 OMEGA EP planar target experiment. The detailed data analysis is still ongoing, and we are planning to conduct more PIC simulations scanning laser intensities (~10^{15} – 10^{17} W/cm^2) and laser speckles to study the LPI and the scaling of the hot electrons.

2.3 Hot electron measurement

As discussed above, Shock ignition (SI) is an alternative inertial confinement fusion (ICF) concept with potential advantages of mitigating hydrodynamic instabilities and reducing the required ignition driver energy. [15-17] In shock ignition, a low-intensity (10^{14} – 10^{15} W/cm^2) laser pulse first compresses the fuel, followed by a high intensity (~ 10^{16} W/cm^2) spike pulse that launches a strong converging shock with an initial shock pressure > 300 Mbar to ignite the fuel. [15,18] However, the energy conversion from the spike laser to the ignition shock remains unclear due to the strong level of laser-plasma instabilities (LPIs) present. Previous simulations predicted that LPI-induced hot electrons with T_{hot} < 150 keV may benefit the full-scale shock ignition with a significant gain increase as well as expand the parameter space for robust ignition designs.

It is thus necessary to characterize the temperature and total energy of these hot electrons to determine their effect on strong shock generation for SI. The hot electron generation can be affected by plasma temperature, scale length, laser intensity and pulse duration, as suggested in previous experiments and simulations. No previous experiments have been completed under conditions with both a laser intensity of 10^{16} W/cm^2 and a large-scale hot plasma. Both conditions were achieved in our experiments in this project. We have also compared the hot electrons generated by infrared (IR) and ultraviolet (UV) lasers to expand the shock ignition design parameters.

I. Experimental setup

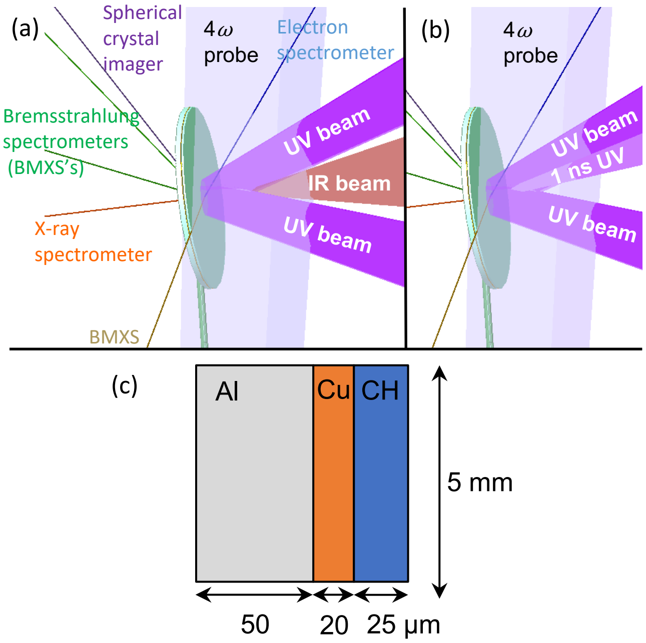

Figure 10: Laser, main diagnostics and target configurations with (a) IR interaction beam and (b) UV interaction beam. Two long-pulse UV beams with the overlapped intensity of 3.6 × 10^{14} W/cm^2 were used to create the large-scale plasma. A 4ω probe diagnostic system was used to characterize the electron density profile. Bremsstrahlung emission spectra were detected by 3 BMXSs. The hot electron excited Cu Ka radiation was measured by a spherical crystal imager and an x-ray spectrometer. (c) is the target configuration with CH ablator facing lasers.

The planar target experiment was performed on the 4-beam OMEGA-EP laser facility. Figure 10 depicts the beam configuration and main diagnostic setup. Two 3ω UV (λ_{UV}= 0.351 μm) laser beams smoothed by 8^{th} order super-Gaussian 750 μm spot size distributed phase plates (SG8-750 DPP) delivered 6.4 kJ total energy with 4-ns square pulses to the target ablation surface with an overlapped average intensity of 3.6× 10^{14} W/cm^2 to create a high temperature (1.4 – 1.9 keV) and long scale-length plasma. The main interaction beam, either a high intensity square pulse UV beam (1.0 ns, 1.4 kJ, *f*/6.5, 2×10^{16} W/cm^2) at 23° off target normal or a normal incident IR beam (~ 100 ps, up to 2.5 kJ, λ_{IR} = 1.054 μm, *f*/3.2), was injected 1.5 ns after the start of the plasma creation pulse. The UV interaction beam was tightly focused with a focal spot size of ~100 μm and a nominal vacuum laser intensity of 10^{16} W/cm^2 at the quarter critical density position ($n_c/4$ = 2.2× 10^{21} cm^{-3}) which is 200 μm above the target surface. The IR beam has a ~300 μm spot at its quarter critical density position (2.5×10^{20} cm^{-3}), 900 μm above target. The average vacuum intensity of the IR beam is up to 2×10^{16} W/cm^2. The quarter critical density positions for the IR and the UV interaction pulses were obtained from simulation results using both the 1D rad-hydro code HYADES [19] with 50% reduced laser energy and 2D FLASH. A 10-ps fourth-harmonic 4ω probe beam [8] (λ_p = 263 nm) was used to diagnose the electron density profile of the coronal plasma. The 4ω probe measurements also captured the propagation dynamics of the main interaction beam including the resultant density perturbation in the large-scale plasma.

2.3 CORONAL PLASMA CONDITION CHARACTERIZATION

To characterize the large coronal plasma, we used the 2D radiation-hydrodynamic FLASH code to simulate the plasma formation and benchmarked the simulation to the experimental AFR images. The FLASH simulations used the same experimental laser and target parameters. Fig. 11(a) shows the FLASH-simulated electron density profile at the end of the UV plasma creation beam (4.0 ns).

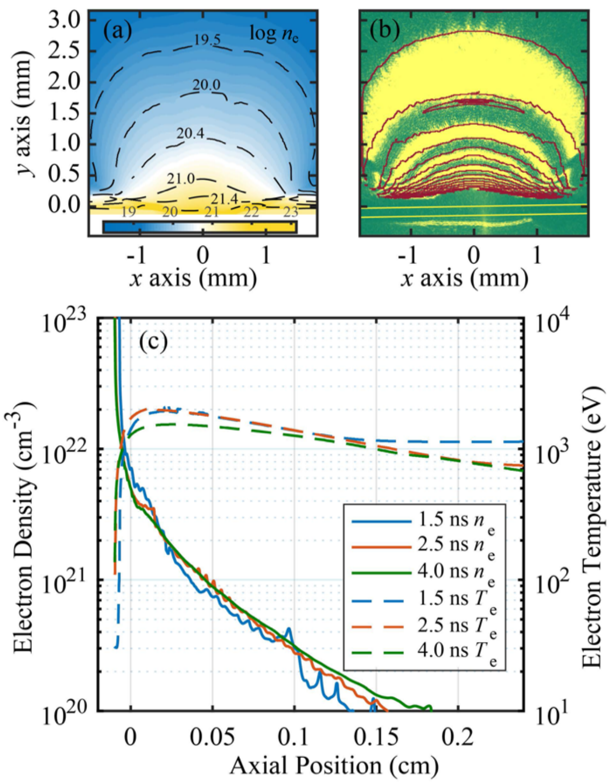

Figure 11: Simulated plasma profiles, experimental and synthetic AFR images: (a) the electron density profile $\log_{10}(n_e)$ at 4.0 ns simulated by FLASH, n_e is in cm^{-3}. The contours with $\log_{10}(n_e)$ = 20, 20.4, 21 and 21.4 represent the surface of $n_c/10$, $n_c/4$ and n_c for IR and the $n_c/4$ for UV; (b) the AFR image at 4.0 ns captured in experiment overlapped with the synthetic AFR image contour simulated from the density profile in (a). The target position before the UV lasers was captured by 4ω probe registration shot and marked with yellow straight lines. y=0 is the original target surface in (a) and (b). (c) FLASH simulated electron density and temperature profiles along the axis normal to the target center at 1.5 ns, 2.5 ns, and 4.0 ns.

In our experiments, electron density profiles were diagnosed by a refraction map of the 4ω probe beam with an Angular Filter Refractometer (AFR) [9]. Fig. 11(b) shows the experimentally measured AFR image (green and yellow) captured at 4.0 ns overlapped by the red contour of a synthetic AFR image. The synthetic AFR image was simulated by the AFR imitation program based on the simulated density profile as shown in Fig 11(a). The synthetic AFR image agrees well with the AFR image in the experiment. The agreement provides confidence in the FLASH simulated plasma conditions for our experiments.

2.3.2 Measurement of the hot electron temperature and total energy

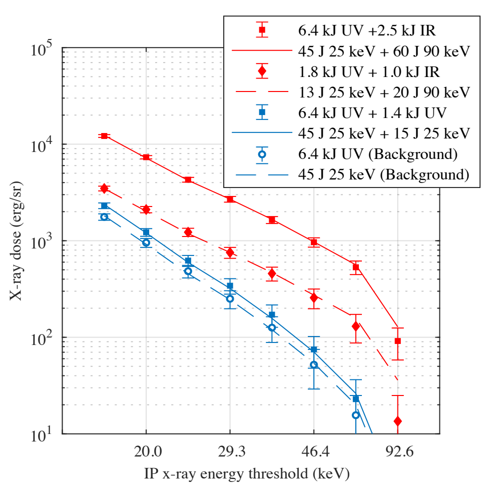

Figure 12: Hard x-ray energy doses on the phosphor layers in BMXS IPs. Points represent the experimental results, and lines represent the best fits from the Monte Carlo simulations. The fitting temperature and the beam energy are labeled.

The temperature and total energy of the hot electrons generated by the UV or IR interaction beam were inferred from the bremsstrahlung x-ray spectra measured by BMXSs. The dots in Figure 12 are the measured x-ray energy doses in the image plate (IP) dosimeters of the BMXS diagnostics. To extract the temperature and total energy of the hot electrons from the measured bremsstrahlung spectra, we fit the synthetic BMXS doses (lines in Fig. 12) to the measured signals. The synthetic BMXS doses are simulated by using the ITS 3.0 Monte-Carlo code. Table 1 lists the fitted hot electron temperatures and total energies.

Table 1: Laser and plasma parameters, the generated hot electron temperature (T_{hot}) and the energy conversion efficiency (E_{hot}/E_L) from the interaction laser to hot electrons. T_e and L_n are the plasma electron temperature and density length scale in the region between $n_c/10$ and $n_c/4$ from FLASH simulations. The intensities were calculated according to the AFR measured spot size on $n_c/4$.

Interaction Laser	Intensity (10^{15} W/cm^2)	T_e (keV)	L_n (μm)	T_{hot} (keV)	E_{hot}/E_L
1.4 kJ UV	10	1.9	330	25	1.1%
0.7 kJ IR	1.5	1.4	460	25	0.7%
1.0 kJ IR	5	1.1	450	90	2.0%
2.5 kJ IR	5	1.4	460	90	2.4%

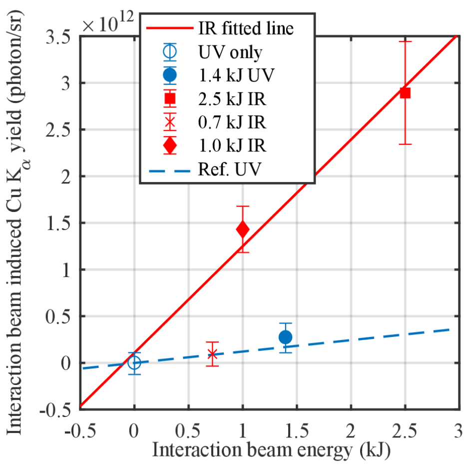

Figure 13: Interaction laser-induced Cu Kα yield in experiments measured by ZVH versus the interaction laser energy. The UV plasma creation laser components of the Cu Kα were linearly energy scaled and subtracted from the original results. The dashed line represents the linear energy scaling of the UV plasma creation lasers. The red solid line is fit to the reference shot and the two high intensity IR interaction shots (diamond and square points). The low intensity IR shot is the red cross.

Besides the bremsstrahlung signal, the measured Cu Kα radiation also independently show hot electron generation from both the UV and the IR interaction lasers. Hot electrons with energies higher than the Cu K-shell binding energy (8.98 keV) reaching the Cu layer can produce Kα x-rays. Figure 13 shows the measured Cu Kα yields as the function of the main interaction laser beam energy, which are the ZVH-measured total yields subtracted by the yield of the UV background shot. The high-intensity UV laser produced Cu Kα with higher yield per laser energy than the plasma creation lasers, shown in the Fig. 13 as the solid blue point compared to the blue dashed line. The error plotted in the figure is the 15% absolute calibration error, but the shot-to-shot error is about 5% (0.5×10^{11} photon/sr) from several identical experiments on OMEGA and OMEGA-EP. Enhanced hot electron generation from the IR interaction laser is also confirmed by the measured Cu Kα x-rays shown as the red line. The red line is the linear fitting from the reference UV point and these 2 high intensity IR points, which give us the Cu Kα yield per unit IR laser energy 6 times as much as the yield per unit laser energy from the UV interaction laser.

In summary, we have demonstrated experimentally for the first time hot electron generation with multiple kilojoule laser energies at shock ignition high intensities in the planar geometry using both the UV and IR lasers in a large-scale plasma. Inferred from the measured bremsstrahlung spectra, the high-intensity IR laser produced hot electrons with higher temperature (90 ± 10 keV) and higher energy conversion efficiency (2.0%–2.5%) than those hot electrons from the UV interaction beam (25±5 keV, ~1.1%). This wavelength dependence is also demonstrated by the measured Cu Kα yield. Besides the wavelength dependence, our experiments also show that the hot electron generation is sensitive to the laser intensity and incident angle. With the more efficient hot electron generation and the demonstrated moderate hot electron temperature, IR lasers could be considered as the spike pulse for the electron-assisted shock ignition. More experiments will be required to further study laser plasma instabilities and the resultant hot electron generation as well as the hot electron energy deposition in the spherical geometry.

2.4.2 Pump-depletion:

Besides the hot electron measurement, we have also characterized the LPI-induced pump-depletion of the UV spike laser to explain the reflectivity discrepancy in simulations and previous experiments. High SBS-induced reflectivity (>50%) were found in some particle-in-cell simulations [20-22], which is not seen in previous experiments [22–29]. However, these simulations were limited by the short time scale and these experiments were limited by either small plasma scale-lengths (L_n<170 μm) or low laser intensities (~10^{15} W/cm^2). In our experiment, we observed unprecedented strong pump-depletion (~100%) that started at the low-density (n_e ~ 0.01 n_c) plasma and progressed into the higher density (n_e > 0.1 n_c) region. This pump-depletion measurement is based on two distinct observations: i) the blast wave generated by the intense laser and ii) the streaked SRS spectrum of the intense laser.

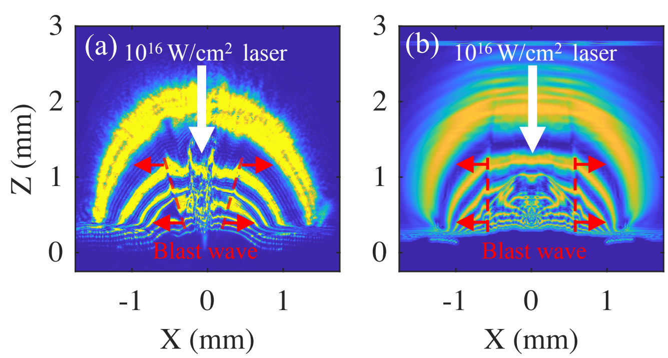

Figure 14. (a) The experimental AFR image; (b) the FLASH simulated AFR image. The target surface is at z = 0. The red dashed lines mark the blast waves. White arrows show the directions of the high intensity UV interaction laser. Red arrows represent the moving directions of the blast waves. The difference of the blast wave shapes (conical vs. cylindrical) can be caused by the LPI-induced pump-depletion.

The shape of the blast waves, shown as the red dashed lines in Fig. 14, indicate that the high intensity laser is strongly pump-depleted. Fig. 14(a) is the experimental AFR image captured at the end of the interaction laser where the blast wave fronts are marked with dashed red lines displaying a conical shape. Fig. 14(b) is the synthetic AFR image based on the FLASH simulated plasma profile, where no LPI-induced pump-depletion is considered. The smaller blast wave diameter at z <1.0 mm in the experiment may be caused by either a lower intensity induced by a steady pump-depletion or a shortened interaction time from a dynamic strong pump-depletion.

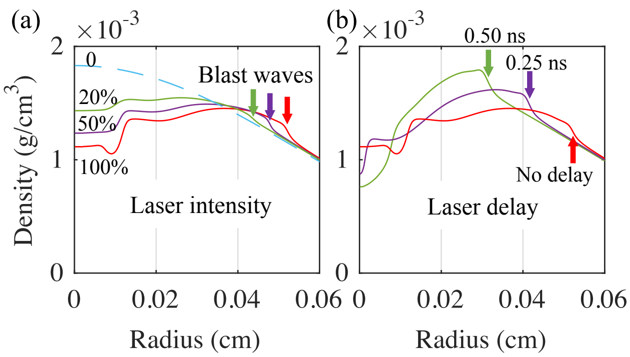

Figure 15. The simulated density profiles after the laser interaction (a) when varying the intensity, and (b) with different laser delays. The arrows mark the fronts of the blast wave.

To verify the effect of the pump-depletion, we performed 1D FLASH simulations with the extracted layer at z = 0.5 mm and scanned the laser intensity (Fig. 15a) and the laser duration (Fig. 15b). As shown in Fig. 14(a), the laser intensity weakly affects the position of the blast wave. When the intensity is further reduced to 5% of the original (profile not shown), the wave front becomes unobservable. No simulations with reduced intensities can reproduce the small but clear blast wave found in the experiment. On the other hand, shorter laser pulse durations can effectively reduce the driven blast wave radius while keeping the wave front observable, as shown in Fig. 14(b). In conclusion, the LPI-induced pump-depletion blocks the first part of the laser. After the pump-depletion, the interaction laser continues to propagate with the same order of the original intensity and generates a small blast wave.

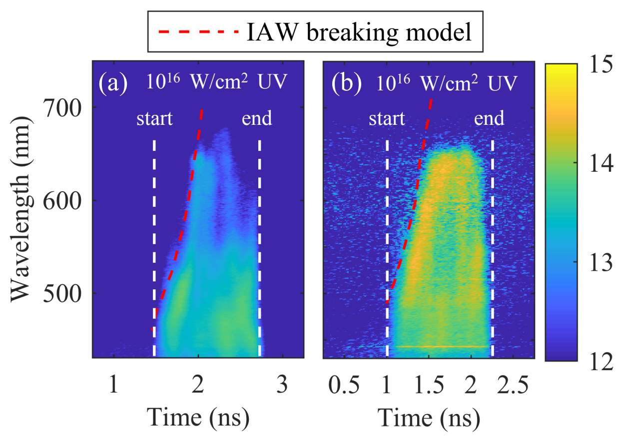

Figure 16. Measured SRS spectra from two experiments in different plasma conditions. (a) The laser and plasma conditions are similar to the blast wave shot (L_n~ 330 μm, T_e~ 1.5 keV); (b) The plasma has higher temperature (2.0 keV) and shorter scale length (260 μm), and the interaction beam is delayed by 1.0 ns. The color bar is in $\log_{10}$ scale. Dashed red lines are pump-depletion positions predicted by the IAW breaking model. T=0 is the start of the low intensity UV lasers.

Furthermore, the time-resolved SRS spectra also show the delayed backscattering light from the deep region. Figure 16 is the two SRS spectra from experiments in different plasma conditions. The image in Fig. 16(a) is under the same conditions as the blast wave image shown above ($L_n \sim 330$ μm, $T_e \sim 1.5$ keV). The SRS signal from $n_e < 0.02\ n_c$ low-density region (λ ~ 450 nm) starts with the high-intensity UV laser. Then the SRS signal from the deeper region (0.02–0.20 n_c) gradually appears. The experiment in Fig. 16(b) has a plasma with smaller $L_n \sim 260$ μm and higher $T_e \sim 2.0$ keV and the interaction laser is delayed by 1.0 ns relative to the initial long pulse beams. Similar to Fig. 16(a), the backscattered SRS light starts at the short wavelength ranging from <500 nm corresponding to $n_e < 0.05 n_c$. After 0.4 ns, the SRS signal extends to 650 nm, where $n_e \sim 0.2\ n_c$. The delay of the SRS signal from the deep region indicates that the first 0.5 ns of the laser pulse is fully depleted at the low density region, which agrees with the slow laser penetration shown in the blast wave analysis.

PIC simulations suggest that the strong pump-depletion is caused by the stimulated Brillouin scattering. However, the simulations are not long enough to show the ns-scale evolution. To explain the dynamics, we have developed an IAW-breaking model to investigate the SBS saturation, which agrees well with the pump-depletion evolution shown as the red dashed line in Fig. 16.

In conclusion, the first experiments to characterize LPI at full-scale shock ignition-relevant laser intensity and plasma conditions have shown evidence of strong pump-depletion of the spike pulse, which is in contrast with previous smaller-scale experiments where SBS was suppressed. This pump-depletion was observed to start at the 0.01–0.02 n_c low-density region and progress into 0.1–0.2 n_c region over the first 0.5 ns of the spike pulse. This dynamic agrees with the IAW-breaking SBS saturation model. This SBS saturation mechanism can explain the reflectivity discrepancy between previous PIC simulations and experiments, where simulations with significantly shorter time-scale overestimated SBS and low SBS is expected in previous experiments with either low intensities or small-scale plasmas. The IAW-breaking may further perturb the plasma and impact LPI, which has not been considered in SI-scheme so far. Furthermore, the strong pump-depletion would inhibit the collisional laser absorption in the megajoule-scale SI scheme, but may benefit electron shock ignition by reducing the TPD generated high energy electrons. Effects of the overlapped beams on LPI and hot electron generation in shock ignition require further investigation.

3. MAJOR ACTIVITIES IN REPORTING PERIOD

The results of the planar and spherical target experiments and the related PIC simulations have been presented at various conferences and workshops as listed below and two manuscripts are in preparation for journal publications.

- M.S. Wei et al., " Hot electron generation and energy coupling in planar experiments with shock ignition high intensity lasers" (Talk), The 58th Annual Meeting of APS DPP, San Jose, CA, Oct. 31 – Nov. 4, 2016
- S. Zhang et al., "Study of hot electron spatial energy deposition in spherical targets relevant to shock ignition" (Talk), The 58th Annual Meeting of APS DPP, San Jose, CA, Oct. 31 – Nov. 4, 2016
- M.S. Wei et al., "Hot Electron Scaling in Long Pulse Laser Plasma Interaction Relevant to Shock Ignition" (Talk), 2017 Stewardship Science Academic Program Symposium, Naperville, IL, April 12 – 13, 2017
- S. Zhang et al., "Study of hot electron spatial energy deposition relevant to shock ignition scheme" (Poster), 2017 Stewardship Science Academic Program Symposium, Naperville, IL, April 12 – 13, 2017
- S. Zhang et al., "Hot Electron Generation and Spatial Energy Deposition by Infrared Laser at Shock Ignition Relevant Intensity" (Poster), 2017 Omega Laser User Group Meeting, Rochester, NY, April 26 – 28, 2017
- J. Li et al., "Particle-in-Cell Simulations of Hot Electron Generation in Laser Plasma Instabilities in Shock Ignition" (Poster), 2017 Omega Laser User Group Meeting, Rochester, NY, April 26 – 28, 2017
- S. Zhang et al., "Hot electron generation and spatial energy deposition by infrared laser at shock ignition relevant intensity" (Talk), The 44th International Conference on Plasma Science, Atlantic City, NJ, May 21 – 25, 2017
- Zhang et al., Experimental study of hot electron generation in shock ignition relevant high-intensity regime with large scale hot plasmas, submitted to PoP

- Zhang et al., Pump-Depletion Dynamics and Saturation of Stimulated Brillouin Scattering in Shock Ignition Relevant Experiments, submitted to PRL
- Li et al., Pump depletion and hot electron generation in long density scale length plasma with shock ignition high intensity laser, submitted to PRE
- S. Zhang et al., “Directional electron beam produced by a 100 picosecond kilojoule infrared laser in shock ignition relevant conditions”, in preparation.

APPENDIX 1: BIBLIOGRAPHY AND REFERENCES CITED

[1] R. Betti et al., *Phys. Rev. Lett.* **98**, 155001 (2007)
[2] R. Betti et al., *J. Phys:Conf. Ser.* **112**, 022024 (2008)
[3] S. Gus'Kov et al., *Phys. Rev. Lett*. **109**, 255004 (2012)
[4] R. Nora et al., *Phys. Rev. Lett.* **114**, 045001 (2015)
[5] W. Theobald et al., *Phys. Plasmas* **22**, 056310 (2015)
[6] C. Stoeckl et al., *Rev. Sci. Instrum.* **83**, 033107 (2012)
[7] L.C. Jarrott et al., *Rev. Sci. Instrum.* **88**, 043110 (2017)
[8] C. Chen et al., *Phys. Plasmas* **16**, 082705 (2009)
[9] C. Stoeckl et al., *Phys. Rev. Lett*. **90**, 235002 (2003)
[10] W. Seka et al., *Phys. Plasmas* **16**, 052701 (2009)
[11] M. Fatenejad et al., *Bulletin of American Physical Society* **57**, BAPS.2012.DPP.CP8.81 (2012). http://meetings.aps.org/link/BAPS.2012.DPP.CP8.81; http://flash.uchicago.edu
[12] J. Allison et al., Nuclear Instruments and Methods A **835**, 186 (2016)
[13] R. G. Hemker, "Particle-in-cell modeling of plasma-based accelerators in two and three dimensions", Ph.D. thesis, University of California, Los Angeles (2000)
[14] R. Fonseca et al., *Lecture Notes in Computer Science* **2331**, 342 (2002)
[15] D. R. Welch et al., *Phys. Plasmas* **13**, 063105 (2006)
[16] R. Betti et al., Phys. Rev. Lett. **98**, 155001 (2007).
[17] D. Batani et al., Nucl. Fusion **54**, 054009 (2014).
[18] S. Atzeni et al., Nucl. Fusion **54**, 54008 (2014).
[19] R. Betti et al., J. Phys. Conf. Ser. **112**, 22024 (2008).
[20] K. S. Anderson et al., Phys. Plasmas **20**, 56312 (2013).
[21] L. J. Waxer et al., Opt. Photonics News **16**, 30 (2005).
[22] J. T. Larsen and S. M. Lane, J. Quant. Spectrosc. Radiat. Transf. **51**, 179 (1994).
[23] D. H. Froula et al., in *Rev. Sci. Instrum.* (2012), p. 10E523.
[24] D. Haberberger et al., Phys. Plasmas **21**, 056304 (2014).
[25] O. Klimo et al., Phys. Plasmas **18**, 082709 (2011).
[26] O. Klimo and V. T. Tikhonchuk, Plasma Phys. Control. Fusion **55**, 095002 (2013).
[27] L. Hao, J. Li, W. D. Liu, R. Yan, and C. Ren, Phys. Plasmas **23**, 042702 (2016).
[28] S. D. Baton et al., Phys. Rev. Lett. **108**, 195002 (2012).
[29] W. Theobald et al., Phys. Plasmas **19**, 102706 (2012).
[30] W. Theobald et al., Phys. Plasmas **22**, 056310 (2015).
[31] C. Goyon et al., Phys. Rev. Lett. **111**, 235006 (2013).
[32] S. D. Baton et al., Phys. Plasmas **24**, 092708 (2017).
[33] S. Depierreux et al., Phys. Rev. Lett. **103**, 115001 (2009).
[34] S. Depierreux et al., Phys. Plasmas **19**, 012705 (2012).

[35] G. Cristoforetti et al., Phys. Plasmas **25**, 012702 (2018).

•